

# Introducing Introspective Transmission for Reflection Characterization in High Frame-Rate Ultrasound Imaging

Gayathri Malamal and Mahesh Raveendranatha Panicker

**Abstract**—In ultrasound imaging, most of the transmit and receive beamforming schemes assume a homogenous diffuse medium and are evaluated based on contrast, temporal and spatial resolutions. However, most medium are constituted by both diffuse and specular regions and the assumption of a homogeneous medium does not hold good in all cases. Eventhough, there are some adaptive beamforming approaches proposed in literature, they are mostly for receive beamforming. This study is aimed at investigating the relevance of transmission schemes in characterizing the diffuse and specular reflections, particularly at high frame rates. The transmit wavefront interaction behavior on the tissue interfaces for two high frame-rate transmission modalities, i.e. conventional synthetic transmit aperture imaging and multi-angle plane-wave imaging, are analyzed for multiple in-vitro and in-vivo radio-frequency datasets. Two novel visualization perspectives are proposed called contour isolines and directivity variance to understand the wave interaction with different tissue interfaces by considering the scalar and vector aspects of the reflected intensities respectively. We also rationalize the relevance of choosing the appropriate receive beamforming scheme according to the transmission modality through a comparison of delay and sum, filtered delay multiply and sum, minimum variance distortionless response, and specular beamforming algorithms. It is found that a synergistic blend of transmit and receive beamforming schemes adaptive to the tissue is inevitable to avoid any misdiagnosis.

**Index Terms**—Contour map, Directivity variance, High frame-rate ultrasound, tissue characterization

## I. INTRODUCTION

ULTRASOUND (US) imaging is popular for its non-invasiveness, lack of ionizing radiation, low cost, and easiness of integrating into bedside monitoring in emergency medicine [1]. The imaging typically follows a pulse-echo approach where a transducer with an array of elements transmits a short acoustic pulse into the tissue of interest. A fraction of US signals are reflected from the tissue due to the acoustic impedance ( $Z$ ) mismatches at various tissue interfaces and are detected by the same set of transducer elements. The signals are digitized, compensated for the round-trip propagation delay, beamformed and converted to an interpretable image format through scan-conversion and log

compression [1], [2].

The reflections from the tissue are broadly diffuse or specular based on the sizes of scatterers relative to the US signal wavelength and  $Z$  mismatches within the tissue [2]. Diffuse reflections occur from scatterers of sizes much smaller than the wavelength of the US signal. Consequently, the backscattering is in multiple directions with a higher spatial distribution of acoustic energy across the transducer array [2], [3]. On the contrary, specular reflections occur when the US signal interacts with tissues/interfaces with high  $Z$  mismatches and dimensions much larger than the signal wavelength [3]. The coherence of the incident signal is preserved and the directivity is governed by the incidence angle of US on the tissue/interface and the tissue/interface orientation. Therefore, the specular reflections may go undetected if directed to outside the transducer receive aperture and lead to misinterpretations especially in musculoskeletal and needle tracking applications [2] – [4]. As the tissue/interface orientation is not inherently unalterable in most cases, the directivity majorly depends on the angle of incidence of US. It is controllable either through appropriate transmission scheme or manipulation in transducer placement which fully relies on the expertise of the sonographer [5]. Hence an introspective transmission, adaptive to the tissue structure or clinical application is what is essential. Moreover, the employed receive beamforming scheme must also be in synchronous with the selected transmit scheme.

Transmit schemes with transducer arrays have been explored in detail in the literature [2], [5]-[11]. Conventional focused transmissions use a fixed focal depth where the acoustic intensity is concentrated for every transmission. The scheme gives better resolution with receive beamforming algorithms but suffers from a low frame rate due to multiple transmissions required with varying focal depths to reconstruct a region of interest owing to narrow insonification [5]. To overcome the frame rate issues, multi-line transmissions have been proposed in [6], [7] where multiple focused beams are transmitted simultaneously. High frame-rate (HFR) imaging has also been achieved by the synthetic transmit aperture (STA) transmission [8], [9] where the transmission is performed element by element of the transducer array. In each transmission, a spherical wave (assuming isotropic transmission) generated by a single transducer scans the entire tissue producing a low-resolution

This work was supported by Department of Science and Technology - Science and Engineering Research Board (ECR/2018/001746) and the Ministry of Education, India.

Gayathri Malamal and Mahesh Raveendranatha Panicker are with the Center for Computational Imaging and Electrical Engineering Department, Indian Institute of Technology, Palakkad, India. (e-mail: 121814001@smail.iitpkd.ac.in; mahesh@iitpkd.ac.in)

image. Dynamic focusing in transmit and receive is achieved by combining the low-resolution images over all the transmissions to form a single high-resolution image [9]. However, the STA scheme suffers from limited penetration depth due to low-energy single element transmissions [10] and tissue motion artifacts [9]. Improvisations of synthetic aperture transmissions have been investigated in literature such as synthetic receive apertures, multi-element transmit/receive sub-apertures, and use of virtual sources to create diverging waves [8], to mitigate the above issues and increase the frame rate. Further, a concept of ultrafast imaging has been introduced in [11] to achieve a very HFR by exciting the full transducer aperture to generate unfocused transmissions and giving giving a wider field of view through plane-waves (PWs). However, the lack of transmit focus results in reduced resolution and contrast which is overcome by synthetically creating a dynamic focus through the coherent compounding of steered PW transmissions with a little compromise on frame rate [10].

The wavefront generated according to the transmit scheme interacts with the tissues, and the reflections directed to within the transducer aperture limit are captured over time [9]-[12] to reconstruct the region of interest. There have been numerous efforts towards developing data-independent and dependent receive beamforming algorithms [12]-[20] to reconstruct the final images from detected reflections. Conventionally, US systems use the data-independent delay and sum (DAS) beamforming with dynamic receive focusing where the geometric delay compensated signals are summed to form the final beamformed signal [12]. DAS has the advantage of simplicity, robustness, and is real-time [12] but suffers from low resolution and off-axis clutter [13] - [15]. To overcome the inherent issues with DAS, data-dependent beamforming schemes based on Capon/Minimum variance distortionless response (MVDR) techniques [16]-[18] have also been investigated. Unlike DAS that uses geometry-based aperture weight estimation, the aperture weights are estimated from the received data for the data-driven schemes. The schemes provide better resolution and clutter rejection, but the high computational complexity restricts the real-time implementation [15]. Further, a non-linear beamforming scheme called filtered delay multiply and sum (F-DMAS) has also been proposed [13]. The delay compensated signals are multiplied in all possible pair-wise combinations (excluding the self-products) and then summed to leverage the spatial coherence of the received signals by inducing a cross-correlation. The beamformed signal is filtered to extract the second harmonic component that is generated from multiplication which results in better resolution and contrast [13]. An efficient improvisation of [13] is proposed in [15] where the temporal products are estimated through convolution which translates to a fast Fourier transform implementation in the frequency domain. However, all the discussed beamforming schemes assume a homogenous diffuse medium. There also exist beamforming schemes that are dedicated to enhancing specular reflections [19], [20]. In the delay and standard deviation beamforming [19], the high standard deviation of specular reflections is exploited to enhance the specular reflections. The specular beamforming (SB) [20] uses Snell's law of reflection and the coherence conservation in reflections to characterize specular reflections and maximize the signal-to-

noise (SNR) ratio. But these suppress diffuse reflections thus restricting it to be a supplementary technique [20]. Hence, a systematic analysis of the transmit and receive beamforming schemes is required from the perspective of the nature of reflections from the medium.

### A. Motivation and Contribution

In this work, an attempt towards investigating the relevance of transmission schemes in characterizing diffuse and specular reflections is presented. Though there has been perpetual work on transmit and receive beamforming schemes and their comparisons, the analyses are on an underlying assumption of a homogenous diffuse medium [12] and are restricted to image quality judgement based on contrast, temporal and spatial resolutions [21]-[23]. However, most tissues are constituted by both diffuse and specular regions and the assumption of a homogeneous medium does not hold in all cases. Considering the transmit wavefront differs for each transmit scheme, an insight into the wavefront interaction on the tissue/interface for each scheme is imperative before deciding on a transmit scheme for a tissue. Moreover, though there are several receive beamforming schemes, dedicated to either diffuse/specular, the significance of selecting the appropriate receive beamforming scheme according to the transmit scheme has never been investigated. In our recent works, we have illustrated the possibilities of coexisting multiple beamforming schemes in a single beamforming unit [24] and diffuse beamforming for specular reflections [25], but without considering the effect of the transmit wavefront. These insights form the motivation of the proposed work and to the best of our knowledge, there is hardly any work in this direction in the literature.

We elucidate this with two HFR transmission modalities 1) Conventional STA imaging and 2) multi-angle PW imaging to respectively enable the analysis of a spherical and planar wavefront behavior with diffuse scatterers and specular interfaces. The schemes also provide a larger field of view with dynamic transmit and receive focusing, a good trade-off between frame rate and image quality. Further, the other existing transmit schemes are limiting cases of STA [26] and therefore the study is easily extendable. Two novel analyses are proposed by characterizing the diffuse and specular reflections in scalar and vector perspectives. The scalar aspect is illustrated by tracing the magnitude of reflections through contour isoline formation across transmissions and the vector aspect is presented by introducing a novel approach called directivity variance (DV). We also rationalize the relevance of choosing the appropriate receive beamforming scheme according to the transmission modality using DAS, F-DMAS, MVDR, and SB receive schemes, to sort of cover the spectrum of existing receive beamforming strategies.

The rest of the paper is organized as follows. Section II presents a brief background discussion of the STA and PW transmission modalities and the receive beamforming schemes DAS, F-DMAS, MVDR, and SB. Section III describes the proposed novel analysis methodologies of contour maps and DV and the experimental setup in details. Section IV presents the detailed discussion of the results. Section VI concludes the paper.

## II. MATERIALS

This section discusses in detail the STA and PW transmit schemes followed by DAS, F-DMAS, MVDR, and SB receive beamforming schemes. A uniform linear array [12], [15] with  $N_c$  elements, a total array width  $L$  and transmit wavelength  $\lambda$  is assumed. The array is placed at the starting depth. The mathematical expressions are shown for a point  $P = (x_p, z_p)$ , in a medium  $K$  with a speed of sound  $c$ . However, this could be extended to other transducer types.

### A. Transmit Schemes

#### 1) Synthetic Transmit Aperture (STA)

In the STA scheme [8], [9], a single element emits a spherical wavefront insonifying the whole field of view constrained by the beam pattern of the transducer. The explanations in this work are for STA with  $N_c$  single element transmissions and full-aperture reception. Each transmission  $j \in [1, N_c]$  has a transmit delay  $\tau_{tx}(j)$  estimated as in (1), where  $x_j$  is the location of the transmit center.

$$\tau_{tx}(j) = \sqrt{z_p^2 + (x_p - x_j)^2}/c, \quad j \in [1, N_c] \quad (1)$$

#### 2) Plane-wave (PW) transmission

In PW transmission, the full aperture is excited to generate a planar wavefront to insonify the whole medium of interest [10], [11]. The unfocused single transmission results in an image with low resolution and SNR which could be improved by creating a synthetic transmit focus through the coherent compounding of images from multiple steered PW transmissions. The  $M$  PW transmissions with inclination angles  $\alpha_T = \{\alpha_1, \alpha_2, \dots, \alpha_M\}$  required for equivalent image quality as of focused transmission are estimated as derived in [10] and is given by,

$$\alpha_T \approx \left\{ \frac{m\lambda}{L} \right\}, \quad m = -\frac{N_c}{2}, \dots, \frac{N_c}{2} - 1 \quad (2)$$

The transmit delay  $\tau_{tx}(j)$  for the point,  $P$  for each transmission  $j \in [1, M]$  is calculated as in (3),

$$\tau_{tx}(j) = (z_p \cos \alpha_j + x_p \sin \alpha_j)/c, \quad j \in [1, M] \quad (3)$$

### B. Receive Beamforming Schemes

The backscattered signals reaching the transducer elements from the medium are digitized and compensated for the round-trip travel time of the wavefront corresponding to every scatterer in the medium. The round-trip travel time is the sum of the transmit and the receive delays corresponding to each scatterer. The transmit delay depends on the employed transmission modality and the receive delay on the geometric distance of each point on the scan-plane to each transducer element. Therefore, the reflected signal at a time instant  $t$ ,  $s_i(t)$  received on the  $i^{th}$  transducer element,  $i \in [1, N_c]$  for the transmission  $j$  has to be compensated by a delay given by (4),

$$\tau_p(i, j) = \tau_{tx}(j) + \tau_{rx}(i) \quad (4)$$

where,  $\tau_p(i, j)$  is the total delay that is the sum of the transmit delay  $\tau_{tx}(j)$  of the  $j^{th}$  transmission and the receive delay  $\tau_{rx}(i)$  for the  $i^{th}$  transducer element. The receive delay is a function of the Euclidean distance of  $P$  from the  $i^{th}$  transducer element placed at  $(x_i, 0)$  as in (5),

$$\tau_{rx}(i) = \sqrt{z_p^2 + (x_p - x_i)^2}/c \quad (5)$$

The delay compensated signals  $s_i(t - \tau_p(i, j))$ ,  $\forall i \in N_c$  are beamformed by applying a beamforming scheme. Further, the beamformed signals from all the transmissions are coherently compounded to obtain the final intensity value of  $P$  as in (6),

$$Y_{bf,P} = \sum_{j=1}^T y_P \quad \begin{array}{l} ; T = N_c \text{ for STA} \\ ; T = M \text{ for PW} \end{array} \quad (6)$$

In this work, a comparative study of the performance of a set of four receive beamforming schemes for the STA and PW transmission modalities is presented. The schemes include a composite of data-independent and dependent techniques, DAS, F-DMAS, MVDR, and SB. A brief discussion on each of them is provided in the below subsections.

#### 1) Delay and Sum (DAS)

The DAS [12] is the most popular digital receive beamforming scheme in US imaging in which the delay compensated signals from all the transducer elements corresponding to every point on the medium are apodized and summed to form the final beamformed signal. Therefore,  $y_P$  in (6) is calculated in DAS as in (7),

$$y_P = \sum_{i=1}^{N_c} W_i s_i(t - \tau_p(i, j)) \quad (7)$$

where  $W_i$  is the apodization weight of the  $i^{th}$  transducer element calculated proportionally to the geometric distance between  $P$  and the  $i^{th}$  transducer element to reduce sidelobes and improve lateral resolution [12], [13]. This makes DAS a data-independent technique. However, appropriate receive aperture must be estimated by defining an accurate  $F$  - number for the transducer considering the directivity of elements as [12].

#### 2) Filtered Delay Multiply and Sum (F-DMAS)

In F-DMAS [14], the delay compensated signals from each point in the medium are multiplied in all possible pairwise possibilities (excluding self-product terms) and combined additively. The multiplication of signals with similar frequency content synthetically creates a baseband and second harmonic in the spectrum, out of which the second harmonics are filtered to obtain the final beamformed signals. The multiplications squares dimensions resulting in a non-zero mean signal and square root operations are applied to rescale the signals without altering the signs. The beamformed signal  $y_P$  in this case, is represented as in (8)-(10).

$$y_P = \sum_{i=1}^{N_c-1} \sum_{l=i+1}^{N_c} s'_i s'_l \quad (8)$$

where,

$$s'_i = \text{sign}(s_i(t - \tau_p(i, j))) \cdot \sqrt{|s_i(t - \tau_p(i, j))|} \quad (9)$$

$$s'_l = \text{sign}(s_l(t - \tau_p(l, j))) \cdot \sqrt{|s_l(t - \tau_p(l, j))|} \quad (10)$$

The multiplications also implicitly induce a spatial autocorrelation that helps to extract the coherence among the delay compensated signals. Consequently, these improve the

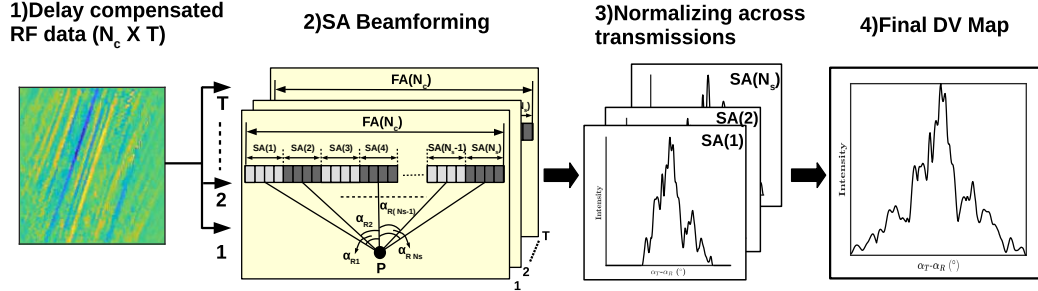


Fig. 1. Illustration of DV approach

lateral resolution and the contrast at the cost of computational overhead. It must be also noted that the spatial autocorrelation introduces an inherent apodization in the F-DMAS topology.

### 3) Minimum Variance Distortionless Response (MVDR)

The MVDR beamforming follows the DAS procedure except that the weights are estimated adaptively from the received data. This work adopts the weight estimation from [16] where the beamformed signal for each point is expressed as a vector by giving a time dependence for the apodization weight for each transmission  $j$  as in (11) – (12).

$$y_P = W_i(t)^H S(t) \quad (11)$$

where,  $H$  denotes the conjugate transpose and  $S(t)$  is,

$$S(t) = \begin{bmatrix} s_i(t - \tau_P(1, j)) \\ s_i(t - \tau_P(2, j)) \\ \vdots \\ s_i(t - \tau_P(N_c, j)) \end{bmatrix} \quad (12)$$

The weights are estimated by minimizing the variance of  $y_P$  as in (13) subjecting it to optimization as in (14) - (16). Here,  $E[\cdot]$  denotes the expectation operator and  $R(t)$  is the spatial covariance matrix of  $y_P$ .

$$E[|y_P|^2] = W_i(t)^H R(t) W_i(t) \quad (13)$$

$$R(t) = E(S(t)S(t)^H) \quad (14)$$

Subject to the optimization problem,

$$\min_{w(t)} W_i(t)^H R(t) W_i(t) \quad (15)$$

Under the constraints,

$$W_i(t)^H a = 1 \quad (16)$$

to estimate the weights as in (17),

$$W_i(t) = \frac{R(t)^{-1}a}{a^H R(t)^{-1}a} \quad (17)$$

where  $a$  is the steering vector and is equal to a vector of ones for already delay compensated data. However, the algorithm has restricted real-time implementation due to the computational complexity involved in the covariance matrix and its inverse calculations [14]-[16].

### 4) Specular Beamforming (SB)

The SB [20] is a dedicated receive beamforming technique for capturing the reflections from planar specular interfaces by leveraging the physics of Snell's law of reflection. The delay compensated data is expressed in terms of transmit angle/angle of incidence of the wavefront  $\alpha_j$  and the reflection receive angle  $\alpha_r$  as in (18) – (19) to detect specularity patterns in the received data and maximize their detection,

$$y_P(\alpha_j, \alpha_r) = s_i(t - \tau_P(\alpha_r, \alpha_j)) \quad (18)$$

$$\alpha_r = \alpha_j - 2\alpha_g \quad (19)$$

where  $\alpha_g$  is the tilt of the reflector. Further, the SNR and the detection probabilities of reflections are enhanced by using a matched filter model of the reflected specular signal. However, in the process, the technique suppresses the diffuse reflections in the medium and has to be always supplemented by other beamforming schemes.

## III. METHODS

In this section, the wavefront-tissue interaction behavior is explored in detail presuming fewer heterogeneous objects in a larger homogenous medium for STA and PW transmit schemes. To be more precise, interactions of spherical and planar wavefronts with tissues are studied with STA and PW schemes, respectively. The reflections from each scatterer point are observed and characterized by viewing from a scalar perspective which considers only the magnitude of reflections and a vector perspective considering both the magnitude and direction. The efficacies and repercussions of the four discussed receive beamforming schemes for the above transmission modalities are also investigated.

### A. Magnitude Tracing - Contour Isolines

The specular reflectors/interfaces typically change the apparent directivity of the transmitted signal according to its orientation and the incident wave angle which is absent in the diffuse reflections. This information is embedded in the signal received in the transducer elements across multiple transmissions. Consider the point  $P$  in the medium  $K$  that belongs to fixed space  $R^2$ . For every transmission  $j$ ,  $P$  has  $N_c$  delay compensated scalar intensity points corresponding to each transducer element that belongs to the level set containing unique  $n$  intensity points  $\{I_1, I_2, \dots, I_n\}$ . The delay compensated scalar intensities corresponding to each transducer element evolves with time or otherwise over every transmission  $j$ , and is expressed as  $\{P \in R^2 \mid f(P) = I\}$ . This forms connected components of similar intensities over time forming isolines or contours [27]. This descriptor aids in tracing the magnitude of reflections by indicating the regions where the connected components in the contour change abruptly providing a physical interpretation of the salient features of the wavefront-tissue interaction in the medium. The features are used to quantify the wavefront patterns corresponding to diffuse and specular reflections.

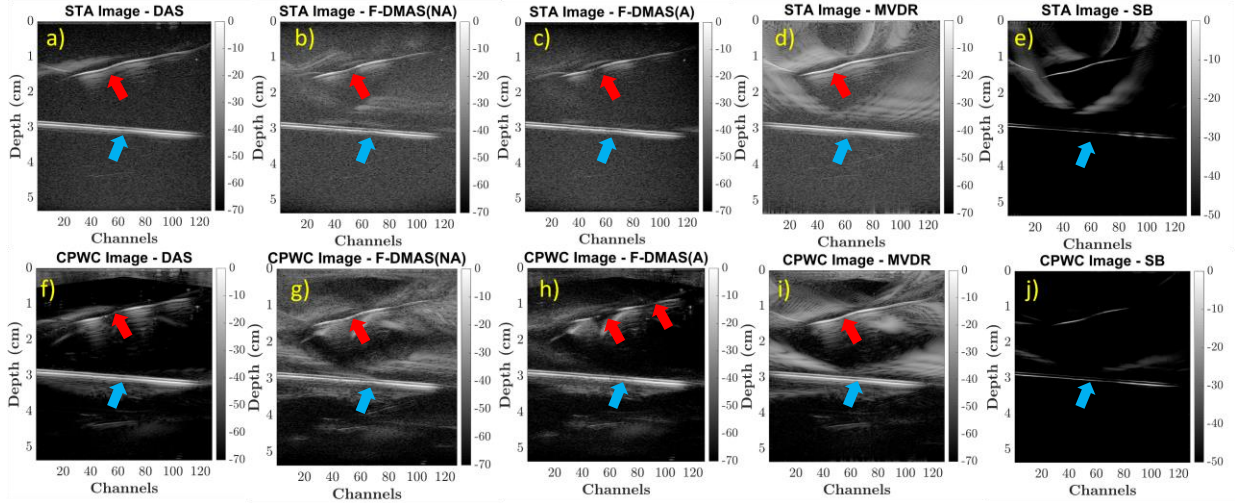


Fig. 2. Beamformed images of gelatin phantom for STA (a – e) and PW (f – h) schemes using DAS, F-DMAS, MVDR and SB techniques as indicated by the plot titles.

### B. Directivity Tracing –Directivity Variance (DV)

The receive beamforming schemes consider only the scalar aspect of the reflected intensity in each transducer element in individual transmissions for estimating the final intensity value of each scatterer point in the medium. This does not account for the reflection directivity as the vector characteristics of reflections from each point  $P$  depend on if  $P$  is diffuse or specular and the angle of the incident wave. In this context, a novel approach of directivity variance (DV) is proposed to characterize the reflections by tracing the variance in their directivity across the transducer aperture with each transmission. The full transducer aperture (FA) with  $N_c$  elements divided into  $N_s$  sub-apertures (SA) (Fig. 1, 2). Each SA makes has a receive angle  $\alpha_{R(n)}$  with  $P$  estimated as in (20) where  $n$  denotes the SA number and  $x_n$  is the SA center.

$$\alpha_{R(n)} = \arctan((x_p - x_n)/z_p) \quad (20)$$

The receive beam is constructed separately for each SA with the intensities across transmissions from the pixel to form a total of  $N_s$  SA beams (Fig. 1, 3)) instead of the conventional single FA beam. This is equivalent to beamforming at different receive angles for every transmission. In the case of diffuse reflections, the intensities across the SAs are similar across transmissions resulting in DV being minimal. But, for specular reflections, the intensities across SAs vary according to the transmit angle and reflector orientation resulting in high DV which is quantified with a variance matrix ( $\Phi$ ) given as in (21), where  $E[\cdot]$  denotes the expectation operator.

$$\Phi = E(SA(n)^2) - (E(SA(n)))^2 \quad \forall n \in N_s \quad (21)$$

A measure of the correlation among SAs is measured statistically as in (22) – (23),

$$\Phi_v = E(\Phi^2) - (E(\Phi))^2 \quad (22)$$

$$\Phi_m = E(\Phi) \quad (23)$$

The maximum value in  $\Phi$  gives the best SA-T pair for the pixel as in (21) and aids to choose appropriate transmissions for the pixel as in (24).

$$\eta = \operatorname{argmax}(\Phi) \quad (24)$$

$$\alpha_T - \alpha_{R\Phi} = \eta \quad (25)$$

This is used to capture the anisotropy of tissues. It is possible that some significant reflections from the tissue may be missed due to improper transmit angle of wavefront or manipulation of the transmit wavefront as seen in many musculoskeletal applications. In such cases, indicating the reflection directions alongside beamformed images, avoids misinterpretations and misdiagnosis. This is achieved by vectorizing the reflection intensity from a pixel with respect to  $\eta$  as in (26), where  $\vec{I}_i$  is the reflection intensity corresponding to the (25) and  $\hat{k}$  and  $\hat{j}$  are the unit vectors corresponding to  $z$  (axial) and  $x$  (lateral) directions.

$$\vec{I}_i = \vec{I}_i \cos \eta_p \hat{k} + \vec{I}_i \sin \eta_p \hat{j} \quad (26)$$

### C. Experimental and Simulation Setup

The experimental RF data acquisitions are conducted with Verasonics Vantage 128 programmable research US system (Verasonics, Inc., Kirkland, WA, USA) with a 128-element linear array transducer (L11-5v) with a pitch of 0.3 mm and width of 3.84 cm. Two *in-vitro* datasets are acquired from, 1) a gelatin phantom (WiP) fabricated by mixing 25 g of food-grade gelatin and 300 ml of water in a plastic container of dimensions 10.5x 10.5 x 5 cm. A 0.8 mm copper wire with small bends is inserted into the phantom with an inclination that mimics a

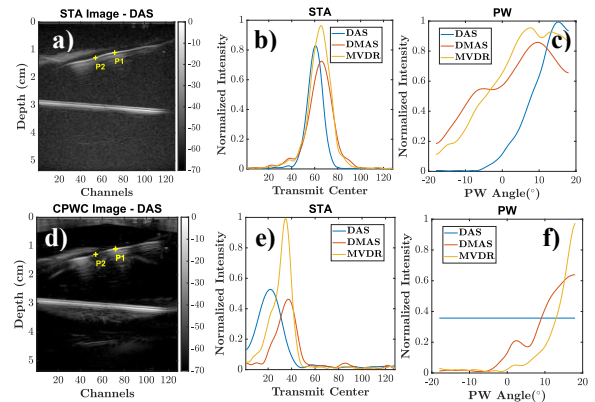


Fig. 3. Illustration of the effect of apodization in the beamsum plots for P1 (b, c) and P2 (e, d)



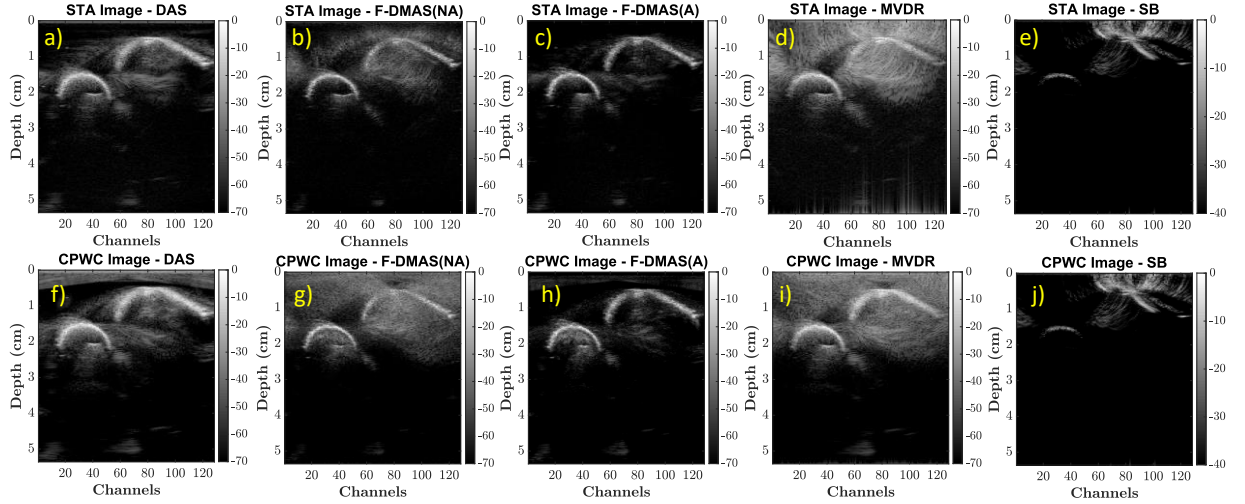


Fig. 4. Beamformed images of bone phantom for STA (a – e) and PW(f– h) schemes using DAS, F-DMAS, MVDR and SB techniques as indicated in plot titles.

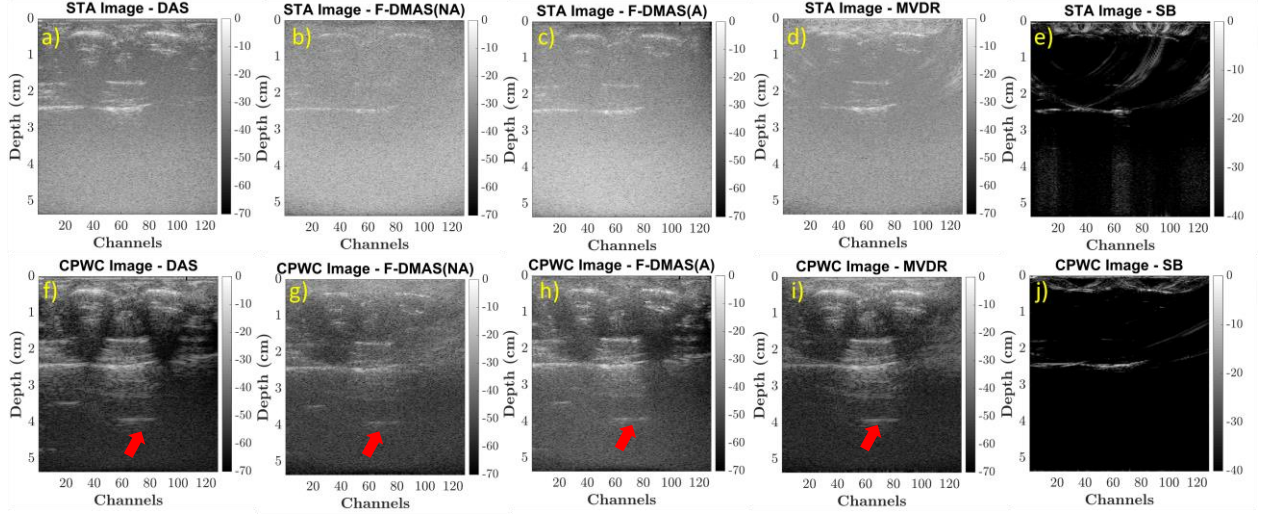


Fig. 5. Beamformed images of the back palm for STA (a – e) and PW(f– h) schemes using DAS, F-DMAS, MVDR and SB techniques as indicated in plot titles.

model with diffuse scatterers and the inserted copper wire behaving as a specular reflector 2) the goat femur and tibia bones (BoP) obtained from the butcher's shop, cleaned and placed in a water bath with the bones adjusted in a standing position with the posterior edge of the tibia and the femur head facing upwards. This is done to capture the peculiar curved specular structure of the posterior tibia and the femur head. In all these cases, the transducer is aligned parallel to the scan surface. Further, an *in-vivo* dataset is acquired from the back palm(BaP) of a healthy volunteer by placing the transducer perpendicular between the metacarpal bones of the index and the middle fingers with the hand in pronation. The dataset exemplifies a heterogeneous medium with bone-soft tissue and air-skin interfaces. Datasets are obtained with a transmit center frequency of 7.6 MHz, sampling frequency of 31.25 MHz, and  $c = 1540$  m/s. STA datasets are acquired for a total of  $N_c = 128$  transmissions and the PW datasets for a total of  $M = 73$  inclination angles between  $-18^\circ$  to  $+18^\circ$  at a  $0.5^\circ$  resolution chosen approximately according to (2). There is no apodization employed in the transmit.

All the datasets are beamformed with DAS, F-DMAS, MVDR, and SB receive beamforming methods to analyze the influence of STA and PW schemes on each receive beamforming scheme using MatlabR2019a (The MathWorks, Natick, MA, USA). For F-DMAS beamforming, the datasets are upsampled by twice the original sampling frequency to obtain the second harmonic at the beamformed output without aliasing, which is further extracted using a bandpass filter [14]. As discussed in Section II B 2), F-DMAS has an inherent apodization, however, in our analysis, the F-DMAS without (F-DMAS(NA)) and with receive apodization (F-DMAS(A)) is also included to provide some interesting insights. A receive apodization using Tukey window with  $F - number = 1.5$  (calculated as in [12]) is considered for DAS and F-DMAS(A). For MVDR beamforming, a subarray length of 32 ( $= N_c/4$ ) [17] is chosen. The final beamformed images are obtained by coherently compounding the individual transmissions to obtain dynamic focus at both the transmit and receive [9], [10] followed by the envelope-detection along with the depth, normalization, and log-compression. The beamformed images for DAS, F-DMAS, and MVDR, are displayed for a dynamic

range of 70 dB. For SB, a lower dynamic range of 40 dB/50 dB is chosen as in [20].

The proposed contour maps and DV approaches are presented for selected points on the beamformed images for 128 STA and 73 PW acquisitions respectively. The DV is illustrated by creating beams for  $N_s = 4$  SAs with each SA having  $N_c/4$  elements for all the datasets. Application of DV for visualizing anisotropy is also illustrated on the WiP dataset.

#### IV. RESULTS AND DISCUSSION

The results and discussions are initiated from the receive beamforming schemes followed by the magnitude and directivity analysis with contour maps and DV approach respectively.

##### A. Influence on receive beamforming schemes

The beamformed images of the gelatin phantom with the gelatin medium behaving as diffuse and the copper wire acting as a planar specular reflector are presented in Fig. 2. In DAS beamforming, a noticeable difference is observed in the wire structure (indicated by red arrows, where some portions of the wire are not captured in PW image) between the STA (Fig. 2 a)) and the PW (Fig. 2 f)) images despite applying the same data-independent apodization weights. This is because, the spherical wave transmissions in STA increases the insonification probability of each point on the wire atleast in some transmissions (particularly from the elements around the vicinity of the point). But such localized interactions are minimal in PW transmissions due to the discretized and pre-decided transmit angles. Due to more localized interactions that result in more distributed reflections in STA, the bends in the wire are captured whereas they are missed out in the PW image (indicated by the red arrow). But in F-DMAS(NA) beamforming (Fig. 2 b, g), the coherence of the delay compensated signals are emphasized consequently enhancing the reflection directivity, and the bends in the wire are captured in both STA and PW schemes. But, applying an additional data-independent apodization distorts the wire structure in PW transmission (red arrows in Fig. 2 h) though the artifacts in the diffuse region have been reduced. This is further highlighted by the data-adaptive MVDR beamforming that captures the wire orientation in both STA and PW, but with increased clutter due to the less diffuse scattering in the medium. To provide a better perception of the influence of apodization, the beamsum across the transmissions for two distinct points on the wire are plotted for DAS, F-DMAS(NA), and MVDR in Fig. 3. For STA (Fig. 3 b, e), the three schemes have converging plots for  $P1$  and  $P2$  due to more localized transmissions. But in PW (Fig. 3 c, f), the beamsum plots have different profiles with DAS being significantly different from F-DMAS(NA) and MVDR especially for  $P2$ . This is because the directive reflections from  $P2$  do not align with the geometry based apodization in DAS. Hence DAS completely misses the reflection but the correlation based apodization of F-DMAS(NA) and data-adaptive apodization in MVDR captures the same. Further, SB provides a finer wire resolution with STA than PW at the cost of suppression of diffuse reflections. However, as the spherical wavefront in STA propagates to a larger depth, it tends to be globally planar and hence exhibits similar behaviour to PW as

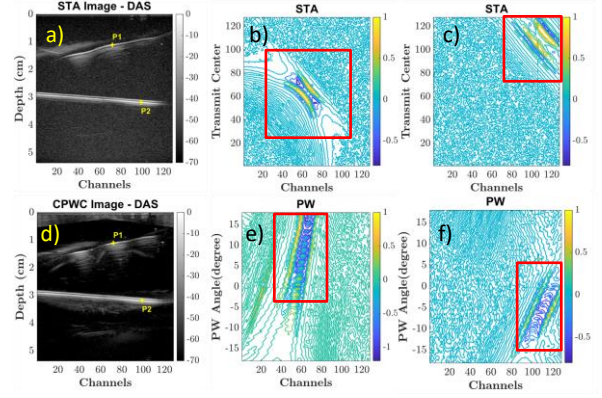


Fig. 6. Contour maps of gelatin phantom for points  $P1$  (b, e) and  $P2$  (c, f). Points  $P1$  and  $P2$  are indicated in the DAS beamformed images of STA and PW in (a, d) respectively.

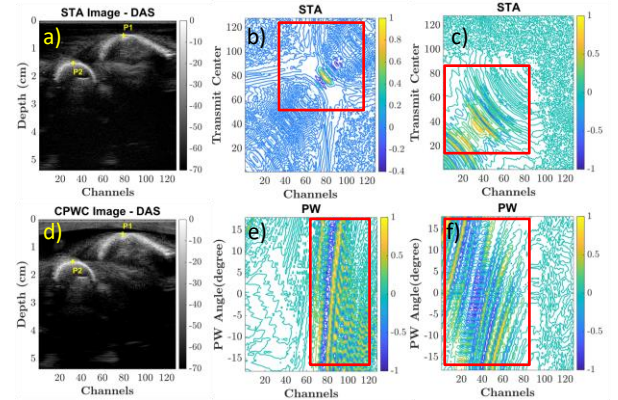


Fig. 7. Contour maps of bone phantom for points  $P1$  (b, e) and  $P2$  (c, f). Points  $P1$  and  $P2$  are indicated in the DAS beamformed images of STA and PW in (a, d) respectively.

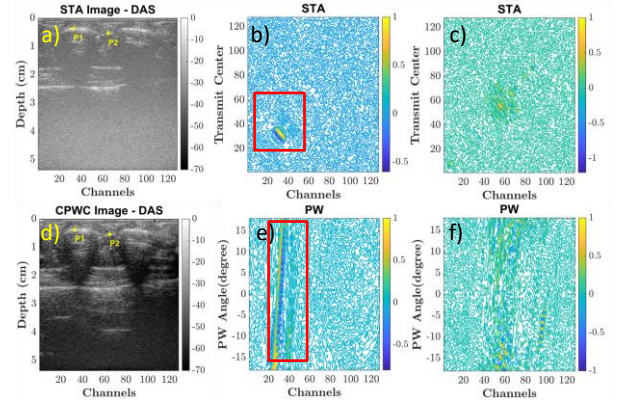


Fig. 8. Contour maps of back palm data for points  $P1$  (b, c) and  $P2$  (c, f). Points  $P1$  and  $P2$  is indicated in the DAS beamformed images of STA and PW in (a, d) respectively.

is evident from the specular reflections from the gelatin-container specular interface (indicated by the blue arrow). This is attributed to the fact that as the spherical wavefront in STA propagates to a larger depth, it tends to be globally planar.

The discussions are now extended to curved specular structures using the bone phantom and back palm datasets. The beamformed images for the bone phantom are presented in Fig

4. The curved structure at  $\sim 0.5$  cm depth is the posterior edge of the tibia and  $\sim 1.5$  cm depth is the femur head. It is interesting to note that, the peculiar curved shapes of the bone structures along with the proximity to the transducer play a role in the response to the wavefront and the extent of exhibiting specularity. In the proximal regions of the transducer, the evolution of the wavefront is in the onset stage. This along with the curved structure of the tibia edge, limits the interaction with the wavefront to very small surface areas resulting in reflections tending to be diffuse and is received majorly by the transducer elements proximal to the pixel points. Hence, the conventional method of data-independent apodization is sufficient. This is evident from the DAS(Fig. 4 a, f) and F-DMAS(A)(Fig. 4 c, h) images where the tibia bone is captured better than the F-DMAS(NA) which adds noise due to the inclusion of spatial correlation of non-relevant aperture. This is further stressed in the SB image (Fig. 4 e, j) where only the femur head is captured despite the tibia being a specular reflector. It is also interesting to note that the data-adaptive STA-MVDR does not outperform data-independent schemes in this case. The beasum plots illustrating the effect of apodization is added in the supplementary document as Fig. 1 to reemphasize the above facts.

The above conclusions are verified with the *in-vivo* back palm dataset (Fig. 5). The two mellow concave structures ( $\sim 0.4$  cm) in the images are the two metal carpal bones of the index and the middle fingers. Contrary to the case of the bone phantom, due to the mellowness in the bone structure a greater surface area interacts with the wavefront. However, this is still limited by the proximity to the transducer. In this case, the specular air-tissue interface is also visible ( $\sim 2.5$  cm). The interesting observation, in this case, is that the multiple reflections (at  $\sim 4$  cm) due to the specular air-tissue interface [28] are observed in PW images (shown in red arrow) and not in the STA images. This is due to the low SNR due to single element transmissions in STA in addition to the attenuation in the tissue. However, in many imaging applications involving US (eg: lung US), the multiple reflections significantly aid the final diagnosis, and employing STA in such scenarios should be therefore carefully decided. For SB, however, this is expected because it emphasizes only high energy specular reflections particularly from planar reflectors, and therefore the low energy multiple reflections are suppressed. The beasum plots illustrating the effect of apodization is added in the supplementary document as Fig. 2.

### B. Magnitude Tracing - Contour Isolines

The scalar aspect of reflections are analysed from contour isoline patterns. Two specular points  $P1$  (on the wire) and  $P2$  (on the back reflection) are chosen on the gelatin phantom as in Fig. 6. The plots highlight the topology of wave propagation in each transmit scheme and the distribution of intensity across transmissions. For the STA, the contour map for  $P1$  shows that the planar specular reflector preserves the spherical wavefront in the reflections whereas, in PW, the planar wavefront is retained. The PW contour maps show that peculiar planar isoline patterns (reflection shift patterns) are formed across transmitting angles  $\sim (0 - +18)^\circ$  (red rectangle) between channels 40-80. This indicates the reflection directivity and indirectly points to the tilt of the surface to which  $P1$  belongs.

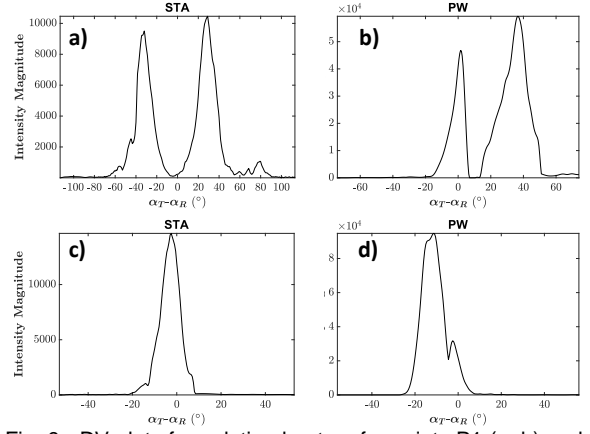


Fig. 9. DV plots for gelatin phantom for points P1 (a, b) and P2 (c, d)

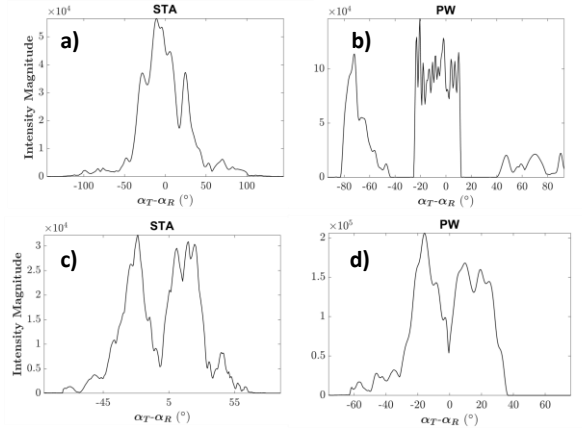


Fig. 10. DV plots for bone phantom for points P1 (a, b) and P2 (c, d)

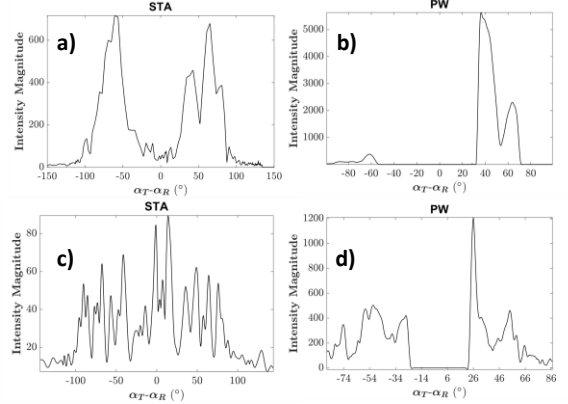


Fig. 11. DV plots for back palm dataset for points P1 (a, b) and P2 (c, d)

TABLE I

Dataset	DV ANALYSIS			
	STA		PW	
	$\Phi_V (10^{10})$	$\Phi_M (10^6)$	$\Phi_V (10^{10})$	$\Phi_M (10^6)$
WiP(P1)	800	2.42	$114 \times 10^4$	77
WiP(P2)	3826	3.1	$913 \times 10^4$	162
BoP(P1)	$177 \times 10^4$	69.3	$486 \times 10^5$	523
BoP(P2)	$180 \times 10^3$	36	$300 \times 10^6$	1535
BaP(P1)	0.03	0.001	76	0.43
BaP(P2)	$\sim 0$	$\sim 0$	$\sim 0$	0.02

A similar observation is also evident for  $P2$  PW contour map (Fig. 6 f) for transmit angles  $\sim (-10 - 0)^\circ$  (red rectangle) across channels 80-128. But for STA(Fig. 6 c) (red rectangle), as the



spherical wavefront in STA traverses to a larger depth, the locally planar wavefront becomes globally planar which in turn results in planar reflections.

As illustrated previously with the bone phantom and the back palm data, the reflected wavefront topology is influenced by the shape of the specular reflectors. This is remphasised in the contour maps in Fig. 7 for bone phantom and Fig. 8 for the back palm dataset. In Fig. 7, two specular points are chosen  $P1$  and  $P2$  on the tibia bone and femur head respectively. For the back palm dataset, a specular point  $P1$  on the metacarpal bone of the middle finger and a point  $P2$  from the diffuse tissue are chosen as in Fig. 8. From the contour maps of  $P1$  for the bone phantom and backpalm dataset in Fig. 7 b, Fig. 8 (b, d) respectively, it is seen that the high energy specular reflections are limited in STA to very few acquisitions due to the proximity to the transducer and limited evolution of the spherical wavefront at these depths. However, in PW contour maps (Fig. 7 e), multiple steered planar wavefronts ( $-18^\circ$  -  $+18^\circ$ ) interact with  $P1$  and produce distributed reflections (visible across channels 60-120). For the point  $P2$  which is at a greater depth than  $P1$  in the bone phantom (Fig. 7 f), it is seen that the reflected wavefront is more diverging with the wavefront in STA tending from spherical to the planar behaviour. The PW reflection also has to be noted for  $P2$ , where the shape of the reflected wavefront is changing slightly from planar to spherical due to the curviness of the surface to which  $P2$  belong. Also, this reduces the area of interaction of the bone surface with the wavefront which creates distributed reflections. The scattered low intensity reflections of the diffuse point  $P2$  (Fig. 8 c, f) of the back palm dataset is also illustrated.

### C. Directivity Tracing – Directivity Variance(DV)

This section discusses the insights from DV approach employing the vector aspect of reflection intensity. The DV plots of the gelatin phantom for the points  $P1$  and  $P2$  of Fig. 6 (a, d) shown in Fig. 9 (a, b) and Fig. 9 (c, d) respectively, show high intensity transmit angle variations as evident through isolated SA beam plots. For  $P1$ , the maximum reflection intensity is centered at transmit-receive angle pairs between  $20$ - $40^\circ$  for both STA and PW. Considering (19), the orientation of the reflector is derived to be between  $10$ - $15^\circ$ . A symmetrical beam to this is also visible about  $0^\circ$  which is obtained for the exact opposite of the above transmit-receive angle pair and further confirms the tilt of the reflector to be in the calculated range. The DV plots for bone phantom and the back palm data in Fig. 10 and Fig. 11 respectively also provide interesting insights. The curviness of the bone structures and proximity to the transducer in both the plots result in intensity getting

distributed across SAs. In the bone phantom, for  $P1$ , it is seen that the peak comes around  $0^\circ$  for both STA and PW. This means that for  $P1$  maximum reflection is emphasized for  $\alpha_T - \alpha_R = 0^\circ$ . Due to the proximity to the transducer, there is higher probability due to the transmissions from the proximity elements in STA or a  $0^\circ$  transmission in PW. Further, for  $P2$ , which is a greater STA and PW have almost identical behaviour as in gelatin phantom. It has to be noted that, in the bone phantom due to the water medium, the attenuation is very less and hence the intensity of reflections remains high. But in the case of the back palm dataset, due to tissue attenuation, in addition to the curviness of the structure and proximity to the transducer, the intensity of reflections are low producing the effect of a diffuse medium. The DV behaviour of a diffuse point is illustrated with the point  $P2$  of the back palm dataset as in Fig. 11 c, d). The reflections spread across the 4 SAs resulting in DV being minimal.

The above discussion is quantitatively expressed through the DV parameters,  $\Phi_v$  and  $\Phi_m$  as shown in Table-I for  $P1$  and  $P2$  of all datasets. Due to large variance in the SA beams, the  $\Phi_v$  and  $\Phi_m$  are very high for the specular points as compared to  $\Phi_v$  and  $\Phi_m$  of the diffuse point  $P2$  of the back palm (BaP( $P2$ )).

The application of DV to visualize anisotropy is illustrated with the gelatin wire phantom in Fig. 12. It is previously illustrated that certain reflections of the wire are missed in DAS beamforming. An region-of-interest (ROI) is selected on the CPWC DAS image around the wire region as in Fig. 12 a). The reflection intensity is vectorized as in (26) and is overlaid on the beamformed image (Fig. 12 b)). The zoomed ROI in Fig. 12 c) clearly shows the presence of reflections (blue arrow) from the wire which is not captured in DAS. Therefore, this could become an indication to the clinician to change transmit/receive beamforming scheme or make manipulations in the transducer placement. The illustrations for bone and backpalm datasets are provided in the supplementary document (Fig. 3 and Fig. 4).

## V. CONCLUSION AND FUTURE SCOPE

In this work, we have investigated and illustrated the importance of introspective transmit schemes adaptive to the tissue using STA and PW in characterizing the diffuse and specular reflections. The reflections are analysed from a scalar and a vector perspective. The scalar aspect is analysed using contour maps and the vector perspective through a novel approach called DV. It is seen that both STA and PW enhance the diffuse reflections if there are an adequate number of transmissions. But, STA performs better than PW for pure and highly specular reflections due to less

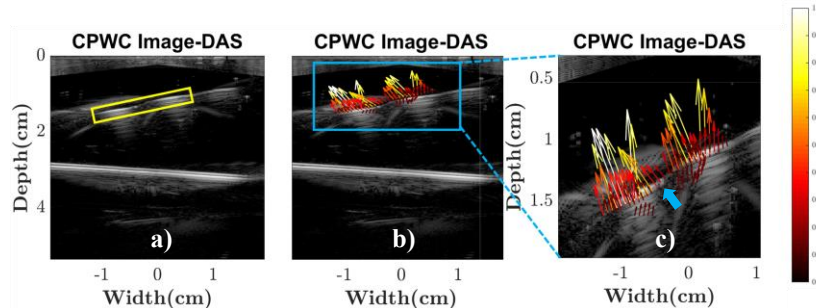


Fig. 12. Illustration of DV approach to visualize anisotropy using the gelatin wire phantom

directionality of the spherical wavefront. However, the low SNR of individual transmissions in STA makes it less prone to multiple reflections that may arise to specular tissue peculiarities. Also, for specular interfaces, either data-independent or dependent beamforming schemes should be decided from the orientation of the interface and proximity to the transducer. It is also noted that SB cannot be employed alone, as it suppresses diffuse reflections and has to be combined with other beamforming schemes. Further, we also illustrate DV as visualization tool by vectorizing the reflection intensity to aid clinicians in identifying anisotropy.

#### ACKNOWLEDGMENT

The authors would like to acknowledge funding from the Department of Science and Technology - Science and Engineering Research Board (DST-SERB ECR/2018/001746) and the Ministry of Education, India. The authors also acknowledge Mr. Madhavanunni A N and Mr. Pisharody Hari Krishnan Gopalakrishnan for their help in data acquisition.

#### REFERENCES

- [1] J. U. Quistgaard, "Signal acquisition and processing in medical diagnostic ultrasound," *IEEE Signal Process. Magazine*, vol. 14, no. 1, pp. 67-74, Jan 1997.
- [2] T. Szabo, *Diagnostic Ultrasound Imaging*, 2nd ed. Academic Press, 2014.
- [3] R. S. Bandaru, A. R. Sornes, J. Hermans, E. Samset and J. D'hooge, "Delay and Standard Deviation Beamforming to Enhance Specular reflections in Ultrasound Imaging," *IEEE Trans. Ultrason., Ferroelectr., Freq. Control*, vol. 63, no. 12, pp. 2057-2068, Dec. 2016.
- [4] A. Rodriguez-Molares, A. Fatemi, L. Løvstakken, and H. Torp, "Specular Beamforming," in *IEEE Trans. Ultrason., Ferroelectr., Freq. Control*, vol. 64, no. 9, pp. 1285-1297, 2017.
- [5] S. Goudarzi, A. Asif and H. Rivaz, "Fast Multi-Focus Ultrasound Image Recovery Using Generative Adversarial Networks," in *IEEE Transactions on Computational Imaging*, vol. 6, pp. 1272-1284, 2020.
- [6] R. Mallart and M. Fink, "Improved imaging rate through simultaneous transmission of several ultrasound beams," *Proc. SPIE*, 1992, vol. 1733, pp. 120 -130.
- [7] G. Matrone, A. Ramalli, A. S. Savoia, P. Tortoli and G. Magenes, "High Frame-Rate, High Resolution Ultrasound Imaging With Multi-Line Transmission and Filtered-Delay Multiply And Sum Beamforming," in *IEEE Transactions on Medical Imaging*, vol. 36, no. 2, pp. 478-486, Feb. 2017, doi: 10.1109/TMI.2016.2615069.
- [8] S. I. Nikolov, "Synthetic aperture tissue and flow ultrasound imaging," Ph.d. dissertation, Dept. of Biomedical Engineering, Ørsted-DTU, Technical University of Denmark, Lyngby, Denmark, 2001.
- [9] J. A. Jensen, S. I. Nikolov, K. L. Gammelmark, and M. H. Pedersen, "Synthetic aperture ultrasound imaging," in *Ultrasonics*, vol. 44, suppl., pp. e5-e15, 2006.
- [10] G. Montaldo, M. Tanter, J. Bercoff, N. Benech and M. Fink, "Coherent plane-wave compounding for very high frame rate ultrasonography and transient elastography," in *IEEE Trans. Ultrason., Ferroelectr., Freq. Control*, vol. 56, no. 3, pp. 489-506, Mar. 2009.
- [11] M. Tanter and M. Fink, "Ultrafast imaging in biomedical ultrasound," in *IEEE Trans. Ultrason., Ferroelectr., Freq. Control*, vol. 61, no. 1, pp. 102-119, Jan. 2014.
- [12] Vincent Perrot, Maxime Polichetti, François Varray, Damien Garcia, "So you think you can DAS? A viewpoint on delay-and-sum beamforming," in *Ultrasonics*, Vol. 111, 106309, 2021.
- [13] K. E. Thomenius, "Evolution of ultrasound beamformers," in *Proc. IEEE Ultrason. Symp.*, pp. 1615-1622, 1996.
- [14] G. Matrone, A. S. Savoia, G. Caliano and G. Magenes, "The delay multiply and sum beamforming algorithm in ultrasound B-mode medical imaging," in *IEEE Trans. Med. Imag.*, vol. 34, no. 4, pp. 940-949, Apr. 2015.
- [15] R. Cohen and Y. C. Eldar, "Sparse Convolutional Beamforming for Ultrasound Imaging," in *IEEE Trans. Ultrason., Ferroelectr., Freq. Control*, vol. 65, no. 12, pp. 2390-2406, Dec. 2018.
- [16] J. F. Synnevag, A. Austeng, and S. Holm, "Adaptive beamforming applied to medical ultrasound imaging," *IEEE Trans. Ultrason., Ferroelectr., Freq. Control*, vol. 54, no. 8, pp. 1606-1613, Aug. 2007.
- [17] J. Synnevag, A. Austeng and S. Holm, "Benefits of minimum-variance beamforming in medical ultrasound imaging," in *IEEE Trans. Ultrason., Ferroelectr., Freq. Control*, vol. 56, no. 9, pp. 1868-1879, Sept. 2009.
- [18] B. M. Asl and A. Mahloojifar, "Minimum variance beamforming combined with adaptive coherence weighting applied to medical ultrasound imaging," *IEEE Trans. Ultrason., Ferroelectr., Freq. Control*, vol. 56, no. 9, pp. 1923-1931, Sep. 2009.
- [19] R. S. Bandaru, A. R. Sornes, J. Hermans, E. Samset and J. D'hooge, "Delay and Standard Deviation Beamforming to Enhance Specular Reflections in Ultrasound Imaging," in *IEEE Trans. Ultrason., Ferroelectr., Freq. Control*, vol. 63, no. 12, pp. 2057-2068, Dec. 2016.
- [20] A. Rodriguez-Molares, A. Fatemi, L. Løvstakken and H. Torp, "Specular Beamforming," in *IEEE Trans. Ultrason., Ferroelectr., Freq. Control*, vol. 64, no. 9, pp. 1285-1297, Sept. 2017.
- [21] E. Roux, F. Varray, L. Petrusca, C. Cachard, P. Tortoli, and H. Liebgott, "Experimental 3-d ultrasound imaging with 2-d sparse arrays using focused and diverging waves," in *Scientific Reports*, vol. 8, no. 9108, pp. 1-12, 2018.
- [22] A. Ortega *et al.*, "A Comparison of the Performance of Different Multiline Transmit Setups for Fast Volumetric Cardiac Ultrasound," in *IEEE Trans. Ultrason., Ferroelectr., Freq. Control*, vol. 63, no. 12, pp. 2082-2091, Dec. 2016.
- [23] M. Orlowska, A. Ramalli, S. Bézy, V. Meacci, J. -U. Voigt and J. D'hooge, "In-Vivo Comparison of Multiline Transmission and Diverging Wave Imaging for High Frame Rate Speckle Tracking Echocardiography," in *IEEE Trans. Ultrason., Ferroelectr., Freq. Control*, 2020.
- [24] L. Tong, H. Gao, H. F. Choi and J. D'hooge, "Comparison of conventional parallel beamforming with plane wave and diverging wave imaging for cardiac applications: a simulation study," in *IEEE Trans. Ultrason., Ferroelectr., Freq. Control*, vol. 59, no. 8, pp. 1654-1663, Aug. 2012.
- [25] G. Malamal and M. R. Panicker, "Towards A Pixel-Level Reconfigurable Digital Beamforming Core for Ultrasound Imaging," *IEEE Trans. Biomed. Circuits Syst.*, vol. 14, no. 3, pp. 570-582, 2020.
- [26] G. Malamal and M. R. Panicker, "Towards Diffuse Beamforming For Specular Reflectors: A Pixel-Level Reflection Tuned Apodization Scheme For Ultrasound Imaging," in *Proc. of ISBI*, pp. 415-418, 2021.
- [27] A. Rodriguez-Molares, H. Torp, B. Denarie and L. Løvstakken, "The angular apodization in coherent plane-wave compounding [Correspondence]," in *IEEE Trans. Ultrason., Ferroelectr., Freq. Control*, vol. 62, no. 11, pp. 2018-2023, Nov. 2015.
- [28] Hamish Carr, Jack Snoeyink, Ulrike Axen, "Computing contour trees in all dimensions," in *Computational Geometry*, Vol. 24, no. 2, pp. 75-94, 2003.
- [29] Shokoohi H, Boniface K. Hand ultrasound: a high-fidelity simulation of lung sliding. *Acad Emerg Med* 2012;19:E1079-83.

# Appendix-I

## IV. RESULTS AND DISCUSSION

### A. Influence on receive beamforming schemes

Fig. 1 show the plots that illustrate the effect of apodization for the points bone phantom. For STA (Fig. 1 b, e), the three schemes have converging plots for  $P1$  due the localized transmissions that result in the reflections directed to the transducer elements closer to  $P1$ . But in the beamsum profile of for PW (Fig. 1 c), the profiles of DAS, F-DMAS (NA) and MVDR are noticeably different from each other. The reflections that are directed to the proximal elements are. Fig. 2 show the plots that illustrate the effect of apodization for the points  $P1$  and  $P2$  on the back palm dataset. In this case, for point  $P1$  (Fig. 2 b, c), the behaviour is similar to that of  $P1$  as in bone phantom for both STA and PW. But for  $P2$ (Fig. 2e, f), which is diffuse, it is seen that all the three schemes show similar beamsum plots due to the diffuse behaviour.

### Directivity Variance(DV) as a visualization tool

The application of DV to visualize the direction of reflections are illustrated with the bone phantom in Fig. 3 and for the back palm dataset in Fig. 4. The images are shown for PW datasets. The selected ROIs are indicated in Fig. 3a and Fig. 4a respectively for the bone phantom and the back palm datasets. The reflection intensity is vectorized as in equation (26) in the paper and is overlaid on the beamformed image (Fig. 3b, Fig. 4b). For better perception, the zoomed ROI is shown in Fig. 3c and Fig. 4c respectively for bone and back palm datasets.

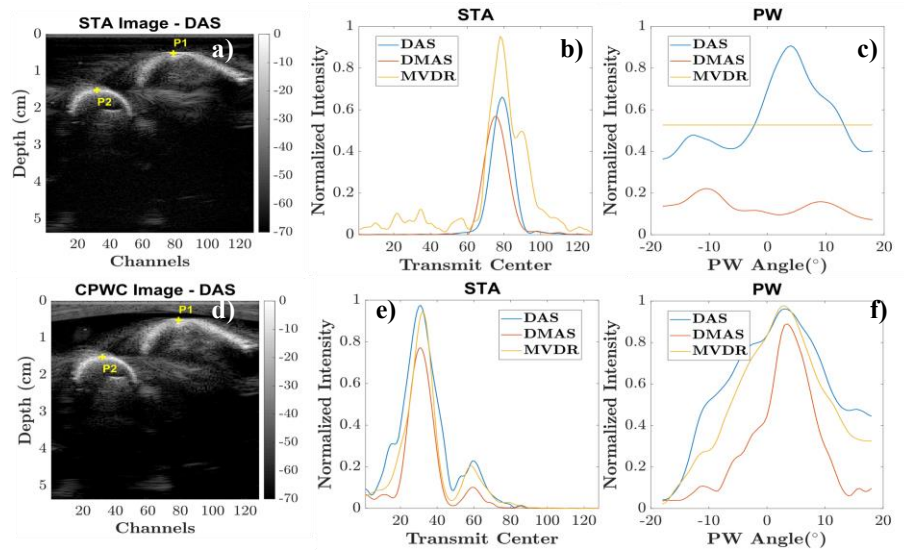


Fig. 1. Illustration of the effect of apodization in the beamsum plots for the bone phantom P1 (b, c) and P2 (e, f)

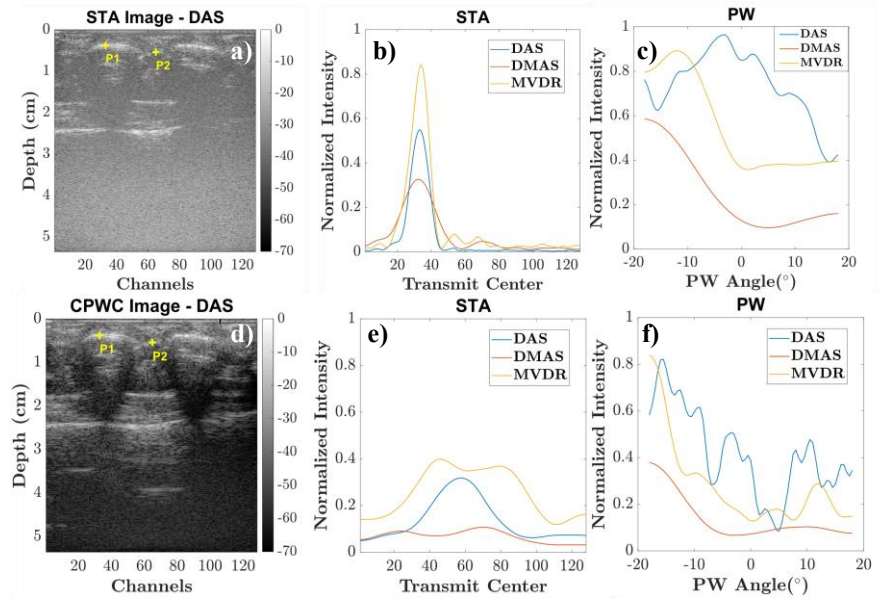


Fig. 2. Illustration of the effect of apodization in the beamforming plots for the back palm dataset P1 (b), c) and P2 (c), d))

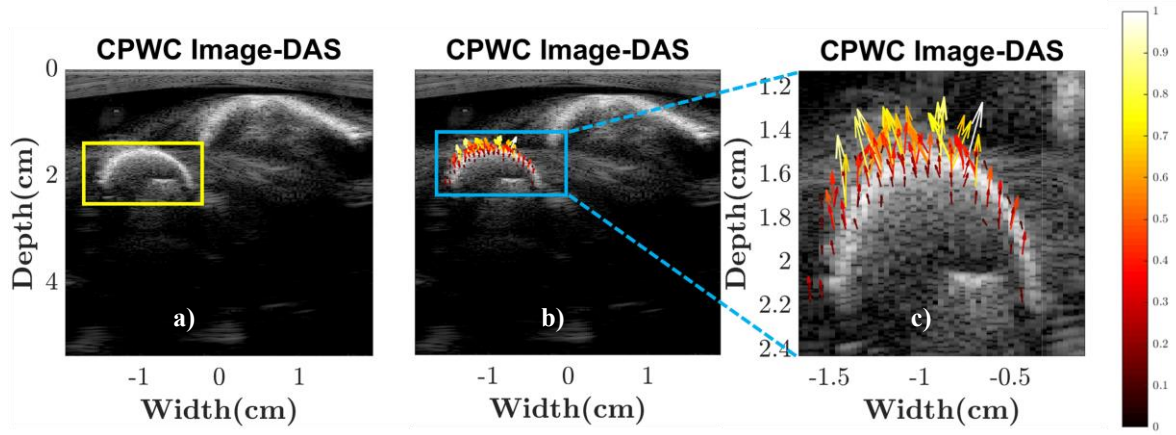


Fig. 3. Illustration of DV approach for visualization in bone phantom

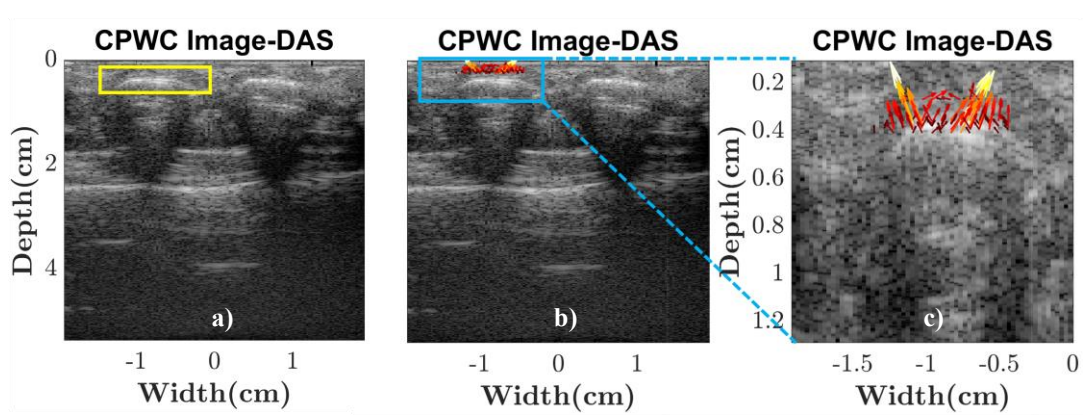


Fig. 4. Illustration of DV approach for visualization in back palm dataset